Received 26 April 2016; | Revised 6 June 2016; | Accepted 6 June 2016

DOI: xxx/xxxx

RESEARCH ARTICLE

Optimal Transportation Meshfree Method in Geotechnical engineering problems under large deformation regime

Pedro Navas*[1,3] | Susana López-Querol[2] | Rena C. Yu[3] | Manuel Pastor[4]

[1]Department of Geotechnical Engineering, Technical University of Catalonia, Campus Nord, Modul D-2, c. Jordi Girona 1-3, 08034 Barcelona, Spain

[2]Department of Civil, Environmental and Geomatic Engineering, University College London, Gower Street, London WC1E 6BT, UK

[3]School of Civil Engineering, University of Castilla La-Mancha, Avda. Camilo Jose Cela s/n, 13071 Ciudad Real, Spain

[4]ETSI Caminos, Canales y Puertos, Universidad Politéctnica de Madrid, c. Prof. Aranguren 3, 28040 Madrid, Spain

Correspondence
*Pedro Navas. Email: penavasal@hotmail.com

Summary

Meshfree methods have been demonstrated as suitable and strong alternatives to the more standard numerical schemes, such as finite elements or finite differences. Moreover, when formulated in a Lagrangian approach, they are appropriate for capturing soil behavior under high-strain levels. In this paper, the Optimal Transportation Meshfree method (OTM) has been applied for the first time to geotechnical problems undergoing large deformations. All the features employed in the current methodology (i.e. F-bar, explicit visco-plastic integration and master-slave contact) are described and validated separately. Finally, the model is applied to the particular case of shallow foundations by using von-Mises and Drucker-Prager yield criteria to find the load at failure in the large deformation regime. The presented methodology is demonstrated to be robust and accurate when solving this type of problems.

KEYWORDS:
Meshfree; OTM; Finite deformation; Shallow Foundations; Drucker-Prager failure criterion; Explicit Newmark central difference scheme

1 | INTRODUCTION

The performance of meshfree methods when large deformation is simulated has improved over the years. The Local Max-Ent (LME) shape functions developed by Arroyo and Ortiz[1] within the Optimal Transportation Meshfree (OTM) framework[2] are one of the most recent advances in this field. This is the methodology adopted within the present research due to its numerous advantages in comparison with other meshfree alternatives, which will be described later on. Since the deformation and velocity fields are interpolated from nodal values using local max-ent shape functions, the Kronecker-delta property at the boundary makes enables the direct imposition of essential boundary conditions [3]. In addition, the parameters related to the Local Maximum-Entropy are obtained efficiently and robustly, regardless of the number of nodes in the support, through a combination of the Newton Raphson method and the Nelder Mead algorithm[4]. Moreover, a finite strain modeling in comparison with some other employments of the OTM methodology in soils in the small strain regime (see[5,6]), has been adopted in this research since it allows us to reach the large deformation regime. This is relevant as the most problematic geotechnical issues cannot be understood without this assumption.

Most of the geotechnical problems concern large compression loadings, exerted through different impactors (for example piles, footings or cones) under high rates. Thus, in this paper several tools are developed in order to be able to model all of these issues. The F-bar methodology is implemented for the first time within the OTM to avoid locking problems when compression occurs. Similarly, when the deformation is large, it is necessary to reconstruct the shape function, which is solved in this research in an elegant manner by using the modified Nelder-Mead algorithm. Finally, contact between bodies is simulated by employing

[0]**Abbreviations:** OTM, Optimal Transportation Meshfree; LME, Local Maximum-Entropy

the contact algorithm proposed by Camacho and Ortiz[7]. It needs to be pointed out that the current work is developed for dry soil in dynamics.

In this research the proposed application to validate the methodology in a geotechnical problem is the modeling of shallow foundations and, particularly, the calculation of the plastic limit load, which can be understood as a theoretical concept that allows us to determine their ultimate design-bearing capacity. The first analytical solutions for calculating plastic limit load were presented by Prandtl[8] and Reissner[9]. Subsequently, a large number of research was carried out in order to calculate the failure value of the loading, several of which were based on frictional models such as the Mohr-Coulomb or the Drucker-Prager constitutive laws. During the last thirty years, these traditional methodologies have been significantly improved due to the advances in computational methods, from finite differences to finite elements.

Numerical approaches permitted the tackling of difficult geometries and the modeling of different types of soils[10,11,12,13,14,15,16]. However, the aforementioned computational methods are restricted to the small strain range. If large deformation problems are to be solved, particle or meshfree methodologies arise as suitable alternatives for simulating such problems[17,18,19]. The name of "meshfree methods" comes from the fact that they do not rely on meshes but on points to approximate functions and differential operators. As examples of these methods, it is worth mentioning the Diffuse Element Method, the Element Free Galerkin Method, the hp-cloud method, the Partition of Unity, the Finite Point Method, the Material Point Model and the Smoothed Particle Hydrodynamics Method. Researchers refer to some of these methods as "particle methods", as the information is associated to a material particle. However, this is not exactly so as these "particles" are indeed nodes carrying information. For instance, a depth integrated SPH model in hydraulics uses nodes associated to columns of fluid where fluid enters and exits the column.

On the other hand, discrete element models such as Discrete Element Method, DEM[20,21], do represent material particles which interact among them. A particle is therefore a real grain of material -or a cluster of them. This is a good choice when large deformation is to be modeled. Nevertheless they have some limitations, i.e. the difficulties with modeling interaction with other phases different from soils (like gasses and/or liquids), the significant number of particles to be modeled or the difficulty in the implementation of boundary conditions.

Furthermore, it is well-known that some difficulties appear when the Mohr-Coulomb failure surface is used in numerical simulations due to the discontinuities of the yield surface. Even though it is not an obstacle for obtaining accurate results[15,22], the Drucker-Prager criterion can overcome that issue by the substitution of the pyramid by a cone. Some other researchers employed this methodology in geotechnical problems and specifically in the solution of bearing capacity of footing loads[23,24,25,26,27,28]. Despite this improvement, it is necessary to solve the corner discontinuity. Sanavia *et al.* proposed an elegant way to predict the stress state before the classical iterator, which entails great savings in terms of computational effort[29,30,31]. For large deformation problems the logarithmic calculation of the small strain tensor proposed by Cuitiño and Ortiz[32] yields much more accurate results. In this paper, we present the application of such approach, previously employed for the von-Mises model with excellent performance, to the Drucker-Prager soil model for the first time.

In the present work, large deformations, in a range up to 25 %, are achieved, which can be considered as the first step towards the simulation of very large deformation problems such as the installation of deep foundations. Moreover, in this paper the shallow foundation is modeled as a different body and the loading is applied with the contact between soil and footing with an algorithm that makes the calculation more realistic. Thus, this paper aims to provide the results of the first application of the OTM method with a Drucker-Prager model for large deformation problems in Geotechnical Engineering, which can be extended to simulate other geotechnical situations such as the installation of piles. Next, the numerical implementation is presented in Section 2, where the Local Max-Ent shape function definition, the contact and F-Bar algorithms and the visco-plastic equations are explained. The validation of the model is presented in Section 3 and the application to shallow foundations in Section 4. The main derived conclusions are summarized in Section 5. Three algorithms are also presented in order to describe the tools carried out for the geotechnical employement of the OTM: algorithm 1 explains the modified Nelder-Mead algorithm, algorithm 2 the Drucker-Prager return mapping and algorithm 3 presents the whole explicit Newmark scheme.

2 | NUMERICAL IMPLEMENTATION

Since there are many different flavours of available meshfree methodologies, an assessment of the state-of-the-art is necessary. Extensive literature is found on the Smooth Particle Hydrodynamics (SPH)[33], also proposed to solve geotechnical problems. For example Blanc and Pastor [19,34] employed a Taylor-Garlerkin discretization to solve dynamic problems, whereas Fan *et al.*[35]

adopted a Drucker-Prager model to simulate the dynamic fragmentation of soils with excellent results. Bui and Fukagawa[36] also worked on the embankment failure but in the pseudo static regime meanwhile. All of these researches required the stabilization of the original methodology. The Material-Point Method (MPM), developed by Sulsky, Chen and Schreyer[37], is utilized by a wide range of researchers, for example Soga *et al.*[38], Alonso and Zabala[39] or Solowski *et al.*[18]. Despite the application of MPM to geotechnical problems is relatively recent, several implementations of this methodology have been already employeed to model rigid body contact in soils[40].

Other meshfree methodologies that have applied contact mechanics in geotechnical applications are the Arbitrarian Lagrangian-Eulerian formulations (ALE), such as the so-called remeshing and interpolation technique by small strain (RITSS) developed by Randolph and *et al.*[41,42,43], the so-called efficient ALE approach (EALE) developed by Nazem and *et al.*[44,45] and the successive built-in implementation of ALE in Abaqus/Explicit, currently known as the Coupled Eulerian-Lagrangian (CEL)[46]. A comparative review of these ALE methods has been recently presented by Wang *et al.*[47]. Finally, the Particle Finite Element Method (PFEM), an updated Lagrangian approach that avoids mesh distortion problems by frequent remeshing, seems suitable to address geotechnical insertion problems[17,48].

The aforementioned Optimal Transportation Meshfree, OTM[2], is based on the principle of maximum entropy[49], with the shape functions developed by Arroyo and Ortiz[1]. Compared to the SPH, the main advantages are the material point sampling, the exact mass transport, the satisfaction of the continuity equation, exact linear and angular momentum conservation, which facilitates the solution of different problems involving spurious modes, tensile instabilities or difficulties in convergence. The main drawback of the MPM is related to the condition of stability of the time integration scheme, which can be solved by increasing the number of material points at the expense of a significant increasing time consumption[50]. In the current work, an explicit Lagrangian framework is established in order to discretize the movement of the domain. The meshfree domain starts with a background mesh in order to locate the different nodes. The new domain is discretized in a nodal set, where the conforming fields are interpolated by means of the Local Max-Ent interpolation[1], as well as the material point set, located in the gravity centers of the elements of the initial background mesh, which contains the material and state variable information. The shape functions are pivotal to the method, since it furnishes a Kronecker-delta property. Moreover, in the OTM approach nodes are convected by the flow[2], what enables the direct imposition of displacement boundary conditions and furnishes automatic compatibility with the contact between different bodies.

In order to be successful in the implementation of the proposed methodology to shallow foundations in large deformation regime, several issues have to be taken into account. For the explicit finite deformation formulation, the book of Bonet and Wood[51] as well as the research by Cuitiño and Ortiz[32] have been herein followed. The calculation of the shape function is made following the algorithm by Arroyo and Ortiz[1] and explicitly for the OTM method by Li, Habbal and Ortiz[2]. An improvement of the calculation of the shape function is required for large deformations, which is presented here as the modified Nelder-Mead algorithm. The visco-plastic algorithm has been based onthe book by De Souza Neto, Owen and Perić[52], the research by Camacho and Ortiz[7] and the implementation of the Drucker-Prager model by Sanavia[29,30]. The current model is comprised of two more components: the contact algorithm by Camacho and Ortiz[7], which is based on the Taylor and Flanagan software, Pronto 2D[53]; and the F-Bar formulation, indispensable to avoid locking problems which has been implemented according to the work of de Souza Neto, Pires and Owen[54], as well as that of Hughes and coworkers[55]. As far as the notations are concerned, bold symbols are employed herein for vectors and matrices, meanwhile regular letters are used for scalar variables.

2.1 | Shape function calculation and Modified Nelder-Mead pseudo-algorithm

Arroyo and Ortiz[1] defined the Local Max-Ent function (LME) as a Pareto set, which is optimal for $\beta \in (0, \infty)$. The optimization provides the shape function of a point $(\boldsymbol{x})$ with respect to the neighborhood $(\boldsymbol{x}_a)$ to use in the calculation of the deformation field, which is as follows:

$$N_a(\boldsymbol{x}) = \frac{\exp\left[-\beta\,|\boldsymbol{x}-\boldsymbol{x}_a|^2 + \boldsymbol{\lambda}^*\cdot(\boldsymbol{x}-\boldsymbol{x}_a)\right]}{Z(\boldsymbol{x},\boldsymbol{\lambda}^*(\boldsymbol{x}))}, \tag{1}$$

where

$$Z(\boldsymbol{x},\boldsymbol{\lambda}) = \sum_{a=1}^{n} \exp\left[-\beta\,|\boldsymbol{x}-\boldsymbol{x}_a|^2 + \boldsymbol{\lambda}\cdot(\boldsymbol{x}-\boldsymbol{x}_a)\right], \tag{2}$$

TABLE 1 Modified Nelder-Mead parameters

ρ	χ	γ	σ	τ
1.0	2.0	0.5	0.5	$1e^{-3}$

and n are the number of the neighbor nodes of the material point ($\boldsymbol{x}$). The first derivatives can be obtained by the following expression:

$$\nabla N_a^* = -N_a^* (\mathbf{J}^*)^{-1} (\boldsymbol{x} - \boldsymbol{x}_a), \tag{3}$$

where $\mathbf{J}$ is the Hessian matrix, defined by:

$$\mathbf{J}(\boldsymbol{x}, \lambda, \beta) = \frac{\partial \mathbf{r}}{\partial \lambda}, \tag{4}$$

$$\begin{aligned} \mathbf{r}(\boldsymbol{x}, \lambda, \beta) &\equiv \partial_\lambda \log Z(\boldsymbol{x}, \lambda) \\ &= \sum_a N_a(\boldsymbol{x}, \lambda, \beta)\,(\boldsymbol{x} - \boldsymbol{x}_a). \end{aligned} \tag{5}$$

The parameter β defines the shape of the neighborhood and is related to the discretization size (or nodal spacing), h, and the constant, γ^*, which controls the locality of the shape functions, as follows,

$$\beta = \frac{\gamma^*}{h^2}. \tag{6}$$

On the other hand, λ is derived from the optimization process required in the calculation of the Local Maximum Entropy shape functions, which is based on the minimization of the function $g(\lambda) = \log Z(\mathbf{x}, \lambda)$ to guarantee the maximum entropy, with $\lambda^*(\mathbf{x})$ as the unique minimizer, being $\square^*$ the optimal values that come from the minimization process. This unconstrained minimization problem with a strictly convex objective function can be solved efficiently and robustly by a combination of the Newton-Raphson method and Nelder-Mead Simplex algorithm[5,1,4]. Unfortunately, for large deformation problems, the update of neighbours is required, which makes the calculation of the parameter λ rather unstable. This instability arises when the three points of the simplex converge to a line as seen in Fig. 1 b. One can verify this fact by calculating the normalized volume, $von(S)$, as Martinez[56] proposes:

$$von(S) = vol\left(\frac{S}{diam(S)}\right) = \frac{|\det(L(S))|}{n!\, diam(S)^n} \tag{7}$$

where S is the simplex, $diam(S)$ is its diameter, v_i, the vertexes of this simplex and $L(S)$ can be defined as:

$$L(S) = [v_1 - v_0 \dots v_n - v_0] \tag{8}$$

Thus, the greater the normalized volume, the better conditioned is the simplex. In Fig. 1 a there are two simplexes with similar volumes and different diameters, but it is worth noting that the first is more convenient computational-wise for the Nelder-Mead algorithm since the convergence is easier. The new step in the algorithm, the spin, seeks to obtain a better simplex, with a better normalized volume, by the rotation of the two worst points with respect to the optimum point. Fig. 1 b presents two simplexes obtained from the two possible rotations around the optimum point. The rest of the points are moved a certain distance, Δd, which is calculated as $diam(S)/10$. The direction of the displacement Δd is different for each of the rotated points, *i.e.* if the first point is moved in the direction x, the second one is rotated in the y direction. Thus, two new different configurations of the simplex are obtained in 2D. The choice between these two possibilities will be defined by the better normalized volume of both simplexes. The number of the possible rotations is $n!$. Thus, in the 3D configuration, 6 different rotated simplex are evaluated, choosing the one with the best normalized volume.

The Nelder-Mead methodology[4] is presented through a flow chart, algorithm 1, in order to understand all the steps, including the new proposed modification. This is different from the one proposed by Martinez *et al.*[56] except employing the same normalized volume. Nelder-Mead parameters, those related to the reshaping of the simplex, are chosen as in the traditional algorithm: $\rho > 0,\ \chi > 1,\ 0 < \gamma < 1,\ 0 < \sigma < 1,\ \chi > \rho$, with ρ being the reflection parameter, χ the expansion one, γ the parameter for the contraction and σ for the shrinkage (see[4] for details). A new tolerance τ is necessary for the admissible normalized volume as well. $dimension + 1$ points are required. Parameters used within this research are shown in Tab. 1 . The new procedure is summarized in Algorithm 1.

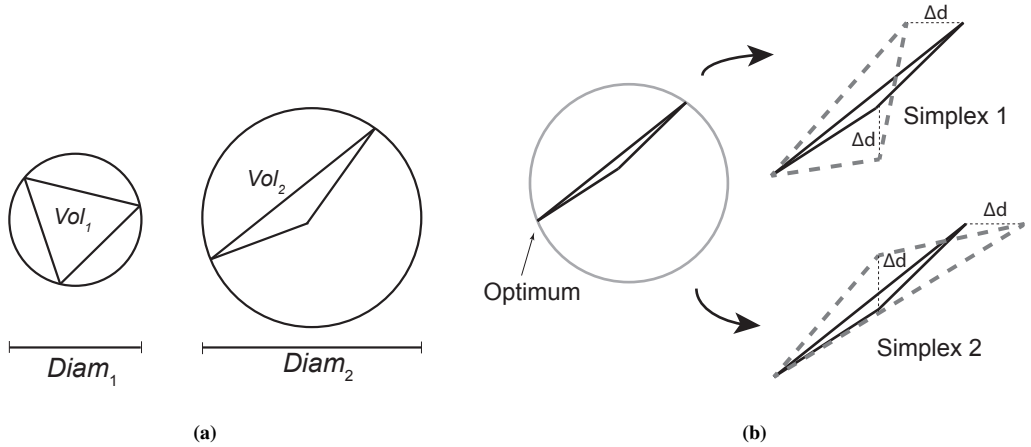

FIGURE 1 a) Two possible simplex with similar volume and different diameter. b) Two possible modifications of the simplex.

2.2 | F-bar formulation

The problems analysed in this paper commonly display numerical instabilities caused by incompressibility, due to the geometry and the properties of the material. Furthermore, the locking problem, which occurs when the pressure locally presents a compression-tension alternation (but keeping a correct global trend), is known to appear in LME schemes[5]. To prevent this problem, the F-bar methodology has been adopted in this research. It consists of the decomposition of the deformation gradient tensor, $\mathbf{F}$, into deviatoric (volume preserving) and volumetric-dilatational parts. Unlike with the small deformation configuration, this split is multiplicative rather than additive. Starting from the work done by De Souza Neto and co-workers[54,57] and Simo *et al.*[58,59], the splitting definition of the deformation gradient is:

$$\mathbf{F} = \mathbf{F}^{vol}\mathbf{F}^{dev} \tag{9}$$

where the determinant of both components yields

$$\det \mathbf{F}^{vol} = \det \mathbf{F} = J, \qquad \det \mathbf{F}^{dev} = 1.$$

The volumetric part of the deformation gradient can be written as:

$$\mathbf{F}^{vol} = J^{1/3}\mathbf{I}.$$

The $\overline{\mathbf{F}}$ tensor is obtained by changing the volumetric part by the volumetric part of the patch,

$$\overline{\mathbf{F}} = \overline{\mathbf{F}}^{vol}\mathbf{F}^{dev}.$$

As the deviatoric part has no volumetric influence, a linear projection, Π must be defined in the dilatational part similar to the projection carried out in the work of Navas *et al.*[5], being:

$$\overline{\mathbf{F}}^{vol} = \Pi(\mathbf{F}^{vol}) = \overline{J}^{1/3}\mathbf{I}. \tag{10}$$

The method proposed by De Souza Neto, Pires and Owen[54] includes the creation of a pre-defined patch $\wp$ or simplex of material points (in our case, see Fig.2), where an average of the volume is computed:

$$v_{patch} = \sum_{i\in\wp} v_i, \qquad V_{patch} = \sum_{i\in\wp} V_i \tag{11}$$

where v_i and V_i denote the volume of material point i in the deformed and the reference configuration, respectively. The projection method leads to a situation where the Jacobian of the patch, $\wp$, is identical to the Jacobian of any material point, e, included in that patch,

$$\overline{J}_e = \frac{v_{patch}}{V_{patch}}. \tag{12}$$

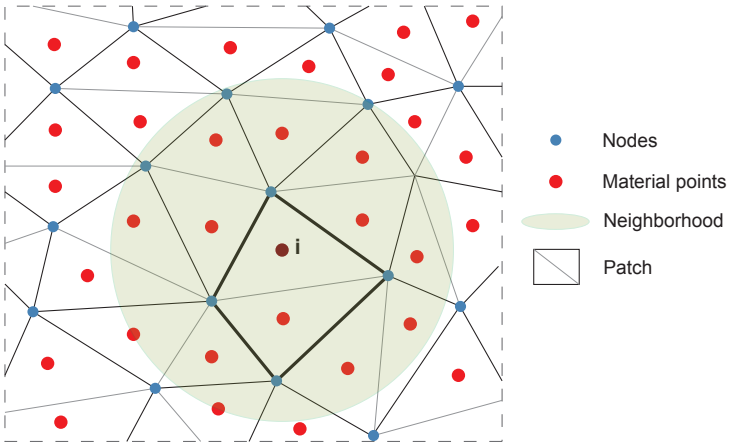

FIGURE 2 Scheme of patch of material points.

Thus, the $\overline{\mathbf{F}}$ yields:

$$\overline{\mathbf{F}} = \left(\frac{\overline{J}_e}{J} \right)^{1/3} \mathbf{F} \tag{13}$$

2.3 | Governing equations and explicit visco-plastic integration

The governing equation of the dynamic problem for a dry soil can be defined by the linear momentum balance equation:

$$\text{div}\, \boldsymbol{\sigma} - \rho \boldsymbol{a} + \rho \boldsymbol{g} = \mathbf{0}. \tag{14}$$

The derivation of the weak form of the problem needs the multiplication by the test function $\delta \boldsymbol{u}$, the virtual displacement, and the integration over the domain. After the application of the Green's Theorem, Equation (14) yields:

$$-\int_{\Omega} \boldsymbol{\sigma} \, : \, \text{grad}\delta \boldsymbol{u} \, \mathrm{d}\Omega + \int_{\Gamma_t} \delta \boldsymbol{u} \cdot \bar{\boldsymbol{t}} \, \mathrm{d}\gamma - \int_{\Omega} \delta \boldsymbol{u} \cdot \rho \boldsymbol{a} \, \mathrm{d}\Omega + \int_{\Omega} \delta \boldsymbol{u} \cdot \rho \boldsymbol{g} \, \mathrm{d}\Omega = 0 \tag{15}$$

where Ω represents the volume of the body and Γ the boundary where tractions are applied. The first term of the equation is defined as the internal forces meanwhile the second and forth conform the external forces. In order to solve this system with the Newmark central difference explicit time integration scheme, Eq. (15) can be rewritten in the matrix form:

$$\boldsymbol{M}\boldsymbol{a}(t) = \boldsymbol{f}^{ext}(t) - \boldsymbol{f}^{int}(\boldsymbol{u}(t)), \tag{16}$$

where $\boldsymbol{M}$ represents the lumped mass matrix and $\boldsymbol{f}^{ext}(t)$ and $\boldsymbol{f}^{int}(\boldsymbol{u}(t))$ are the external and internal forces, respectively. To solve this system with an explicit scheme, it is necessary to follow the traditional predictor-corrector algorithm, which has been enhanced in order to achieve good performance in the geotechnical problems presented in this research. The visco-plastic algorithm is included in an explicit model developed to simulate large deformation problems. Some of the cases we show in this paper cover a strain ranging between 10 and 25 percent. By using the stretch, the eigenvalues of the right Cauchy-Green deformation tensor λ_1, λ_2 and λ_3, the neighborhood of the shape function can be enlarged. This fact allows us to model large deformation problems since the new location of material points and nodes defines new values of the shape function. The employed pseudo-algorithm, where k and $k+1$ are the previous and the current step, is summarized in Algorithm 2.

For the plastic algorithm, the Sanavia Drucker-Prager model has been employed[29,30]. The main advantage of this method is its less computational effort, as it is possible to predict in which region, cone or apex, the stress state is located, before calculating the plastic strain. The parameters of the plastic implementation are the shear modulus, G, the bulk modulus, K, Poisson's ratio, ν, the reference and current cohesion, c_0 and c_{k+1}, the reference plastic strain ε_0, and the hardening exponent, n. In addition, the Perzyna visco-plastic model is added in order to model this behavior as well. This model employs the

TABLE 2 Drucker-Prager parameters

	Plane strain	Outer cone
α_F	$\frac{\tan\phi}{\sqrt{(3+4\tan^2\phi)}}\sqrt{\frac{2}{3}}$	$\frac{2\sin\phi}{3-\sin\phi}\sqrt{\frac{2}{3}}$
α_Q	$\frac{\tan\psi}{\sqrt{(3+4\tan^2\psi)}}\sqrt{\frac{2}{3}}$	$\frac{2\sin\psi}{3-\sin\psi}\sqrt{\frac{2}{3}}$
β	$\frac{3}{\sqrt{(3+4\tan^2\phi)}}\sqrt{\frac{2}{3}}$	$\frac{6\cos\phi}{3-\sin\phi}\sqrt{\frac{2}{3}}$

viscosity-related parameter μ [s] and the rate-sensitivity parameter, ϵ, which ranges from 0 to 1.

It is necessary to calculate the Drucker-Prager parameters from the friction ϕ and dilatancy ψ angles. The application of this methodology is done for 2D plane strain problems, thus the plane strain parameters are used. However, some of the solved validation problems presented in this paper have been compared with Ansys[60]. In order to do so, we need the outer cone parameters, which is the solution that Ansys provides. The outer cone is related to the cone which circumscribe the external edges of the Mohr-Coulomb plastic region. Both types of parameters are presented in Tab.2 . The implementation of this variant of the Drucker-Prager flow rule is depicted in Algorithm 3.

2.4 | Master-slave contact algorithm

The contact algorithm employed in this research is based on that of Camacho and Ortiz[7], which was inspired from that of Taylor and Flanagan in the software Pronto 2D[53]. The aforementioned contact algorithm is purely node-based and does not use approximation functions. The bodies involved in the contact can be rigid or deformable, considering their surfaces as master and slave respectively, which are labeled in Fig. 3 and the equations in this Section as m and s. The different nodes belonging to the master and slave surfaces are denoted with the sub-index k and j, respectively. Thus, $a_{m,k}$ represents the acceleration of the node k of the master surface. As mentioned in Section 2, we first calculate the predictor nodal positions by assuming no contact, which leads to a penetration, $\delta_{s,j}$. The mentioned penetration results in a contact force, P_s:

$$P_{s,j} = \frac{2M_{s,j}\delta_{s,j}}{\Delta t^2} \tag{17}$$

The accelerations in the normal direction depend on these contact forces and the distances between the penetration point and the nodes where the accelerations are applied:

$$a^{norm}_{m,k} = \frac{\sum_j w_{s\to m,j} P_{s,j}}{M_{m,k} + \sum_j w_{s\to m,j} M_{s,j}} \tag{18}$$

$$a^{norm}_{s,j} = \sum_k w_{m\to s,k} a^{norm}_{m,k} - \frac{P_{s,j}}{M_{s,j}} \tag{19}$$

where $w_{s\to m,j}$ and $w_{m\to s,k}$ are weights dependent on position, with $d_{k\to j}$ being the distance between the node k and the node j:

$$w_{s\to m,j} = \frac{\frac{1}{d_{k\to j}}}{\sum_s \frac{1}{d_{k\to s}}} \tag{20}$$

Tangential acceleration depends on a Coulomb friction model. In its calculation, it is necessary to determine the tangential component of the predicted relative velocity between master and slave nodes. A unit tangent vector, $\mathbf{t}$, is employed in this calculation:

$$\Delta v_{s,j} = \mathbf{t} \cdot \left(\mathbf{v}^{pred}_{s,j} - \sum_k w_{m\to s,k} \mathbf{v}^{pred}_{m,k} \right) \tag{21}$$

The tangential force to cancel the tangential velocity is provided by:

$$F^S_{s,j} = -\frac{M_{s,j}\Delta v_{s,j}}{\Delta t} \tag{22}$$

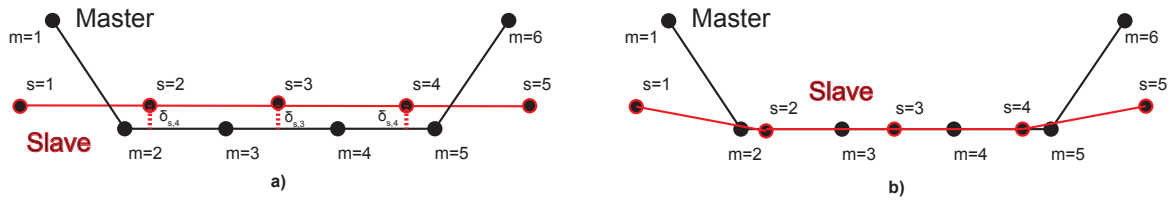

FIGURE 3 Scheme of master and slave boundaries in the predictor (a) and after contact (b) phases.

However, the force exerted by the master surface cannot exceed the maximum frictional resistance, which is calculated taking into account the normal contact force. The normal component of the corrected acceleration is as follows:

$$N_{s,j} = \left(M_{s,j} a^{norm}_{s,j} \right) \mathbf{n} \tag{23}$$

Thus, the tangential acceleration is calculated as:

$$a^{tan}_{s,j} = \frac{F^{tan}_{s,j}}{M_{s,j}} = \frac{F^{S}_{s,j}}{|F^{S}_{s,j}| M_{s,j}} \min \left(\mu N_{s,j}, |F^{S}_{s,j}| \right) \tag{24}$$

$$a^{tan}_{m,k} = -\frac{\sum w_{s \to m,j} F^{tan}_{s,j}}{M_{m,k}} \tag{25}$$

This yields the final acceleration vector as:

$$\mathbf{a} = \mathbf{a}^{pred} + a^{norm} \mathbf{n} + a^{tan} \mathbf{t} \tag{26}$$

3 | MODEL VALIDATION

In this Section, the validations for several aspects of the implemented methodology are presented. First, the F-bar formulation is illustrated by the classic Cook's membrane problem and the compression of a rubber block. Next, the von-Mises and Drucker-Prager failure criteria are validated with the dynamic problem of a square plate loaded in eights steps and two shear problems respectively. Finally, the efficiency of the master-slave contact algorithm is demonstrated through the Taylor bar problem.

3.1 | Validation of the F-bar formulation

The Cook's membrane problem consists of a tapered panel, clamped at one side and subjected to a uniform shear load on the opposite site. It is often used to test the nearly incompressible formulation under combined bending and shear. The material properties employed in this example are $E = 240.565$ MPa and $\nu = 0.49999$. The loading was $F = 100N$ and the geometry is shown in Fig. 4 a. Such a problem has been solved by many authors (see [61,62] for details) and recently by Hughes and coworkers [55] through a B-bar or F-bar projection, by Hauret, Kuhl and Ortiz [63] via diamond elements and by Artioli, Castellazzi and Krysl [64] employing assumed strain NICE (Nodally Integrated Continuum Element) formulation for elasto-plastic applications. Navas *et al.* presented this problem with the first implementation of the B-bar method with LME shape functions [5,6]. In this case, Neo-Hookean non-linear elasticity was employed.

The result seeks an asymptotic vertical displacement at the right-upper corner (point P in Fig. 4 a). In Fig. 4 b the convergence rates of the proposed methodology in the cases with or without F-bar are shown. These results have been also compared with the ones obtained using the B-bar methodology by Navas *et al.* [5] with also Local Max-Ent meshfree shape functions. Note that, when the number of divisions reaches 16 per side, the vertical displacement at P is already about 95% of the asymptotic value similarly to the results obtained with the B-bar methodology. The obtained solutions for the distribution of the hydrostatic pressure are compared in Figs. 4 c-d.

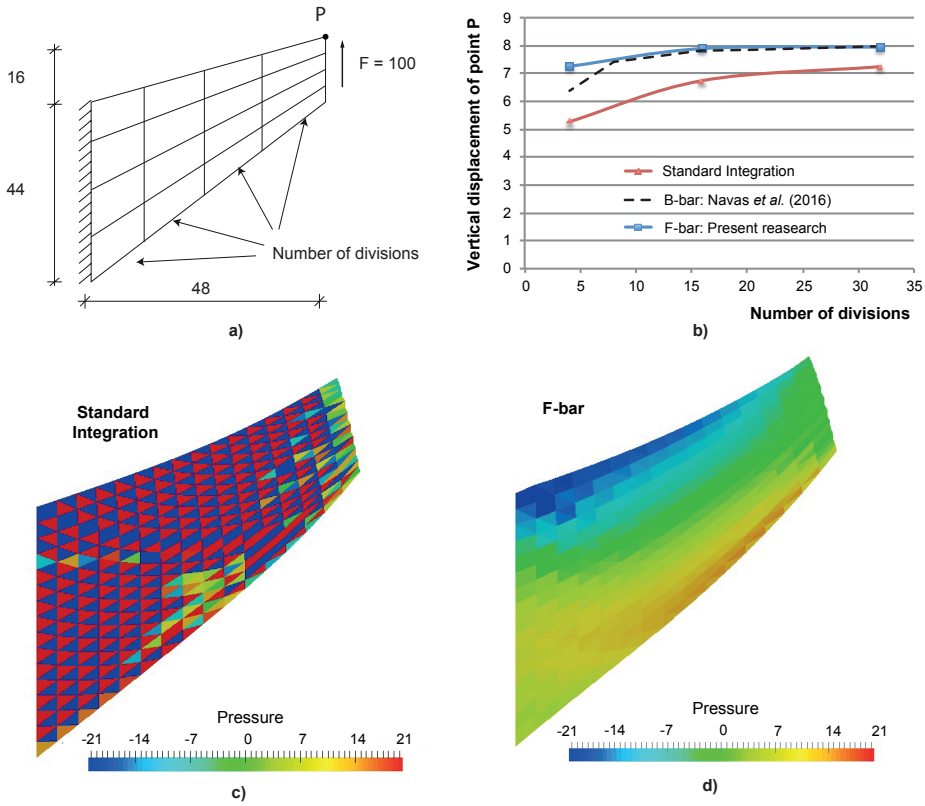

FIGURE 4 The plain strain Cook's membrane problem: a) geometry, loading and boundary conditions; b) Vertical displacement of point P; and Distribution of the pressure c) without and d) with F-Bar integration.

The second example consists of the plane strain analysis of a rectangular rubber block section subjected to compression at the top, as shown in Fig. 5 a. This problem was previously presented by Crisfield *et al.*[65] and can also be compared with De Souza Neto *et al.*[54]. In that case, a Mooney-Rivlin material was adopted, with a value of the bulk modulus, K, of 10^5 Pa, Poisson's ratio, ν, of 0.4999, the corresponding Young's modulus is equal to 60 Pa. In our case, a Neo-Hookean material is adopted. The goal of this second verification is to assess the suitability of the presented methodology for very large deformations.

In Fig.5 b-d, solutions of a 25% compression are shown for three different integration approaches. First of all, the result obtained with standard integration for triangles is presented, displaying unstable behaviour. By contrast, the F-Bar solutions for quadrilateral and triangles present a much smoother solution, similar in both cases. These results are in accordance with those proposed by De Souza Neto *et al.*[54], as can be seen from the figure.

For the same problem, a higher deformation has been calculated using the presented methodology. By utilizing a remapping algorithm, 50% compression can be reached, see Fig.6 . This solution is not attainable without the combination of the F-Bar integration and a very accurate remapping algorithm, using the aforementioned modified Nelder-Mead algorithm.

3.2 | Dynamic behavior of a square plate in a von-Mises material

The presented model is compared with the Ansys solutions in order to assess the performance of both methods. The first problem, presented in the Ansys manual, consists of the evolution of the stress after different imposed displacements on a square plate using the von-Mises yield criterion.

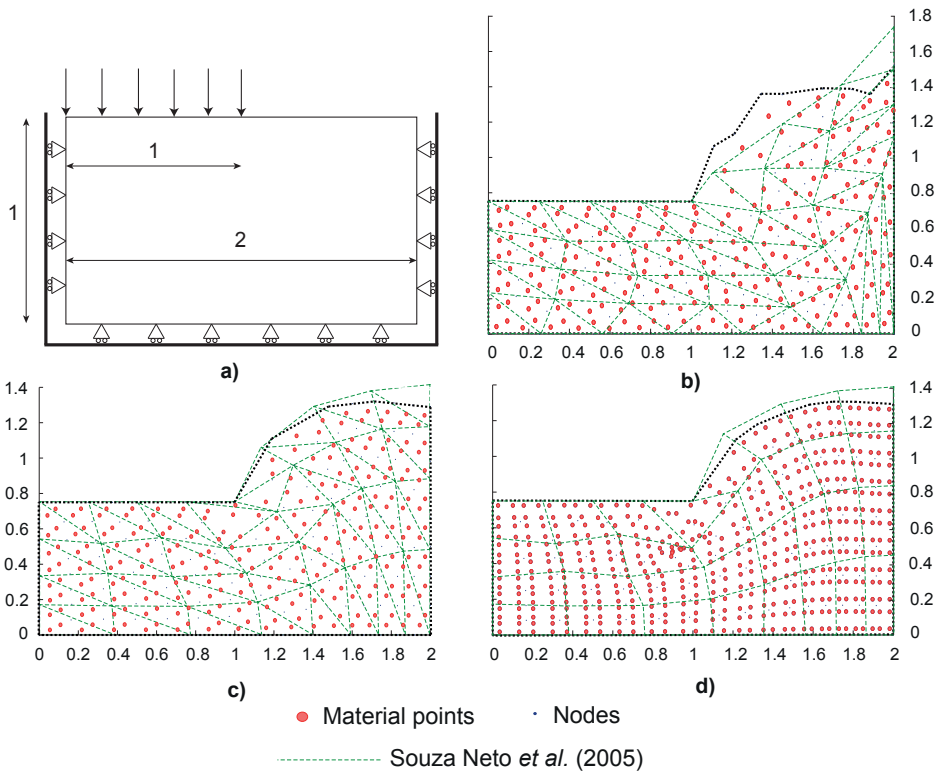

FIGURE 5 The rubber block problem: a) geometry, loading and boundary conditions (dimensions in m); b) 25% of compression in a triangular standard integration; c) 25% of compression in a triangular F-Bar integration; d) 25% of compression in a quadrilateral F-Bar integration;

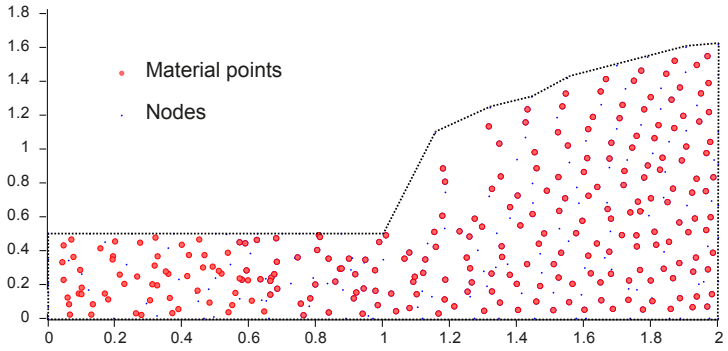

FIGURE 6 The rubber block problem: 50% of compression in a triangular discretization with F-Bar integration.

In Fig.7 , the geometry, material parameters and loading conditions of the problem are presented. Eight loading steps are simulated by extending different boundaries of the plate as shown in the figure.

In order to validate the implemented Local Maximum Entropy meshfree method, the obtained results are compared with those obtained with Ansys. In our case, at point P (top right corner) the evolution of the stress is plotted out in Fig.8 . The numerical results fit rather well. It can be observed how the LME results are smoother than the others.

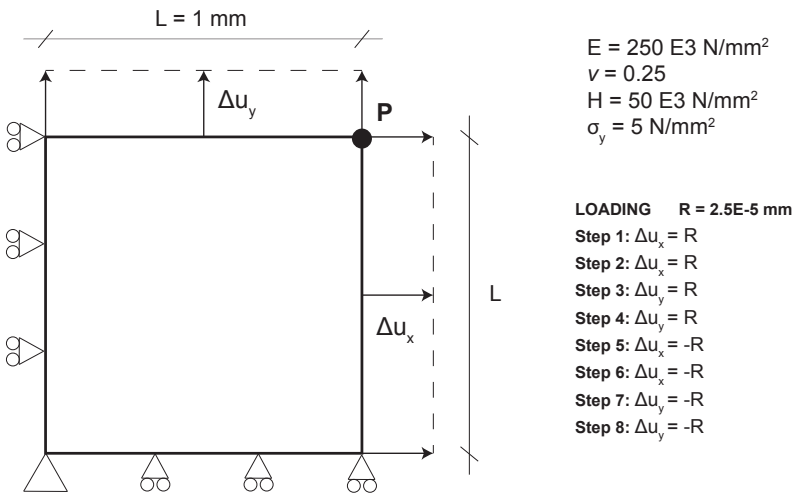

FIGURE 7 Geometry, material parameters and loading condition of the dynamic plasticity problem along a square plate.

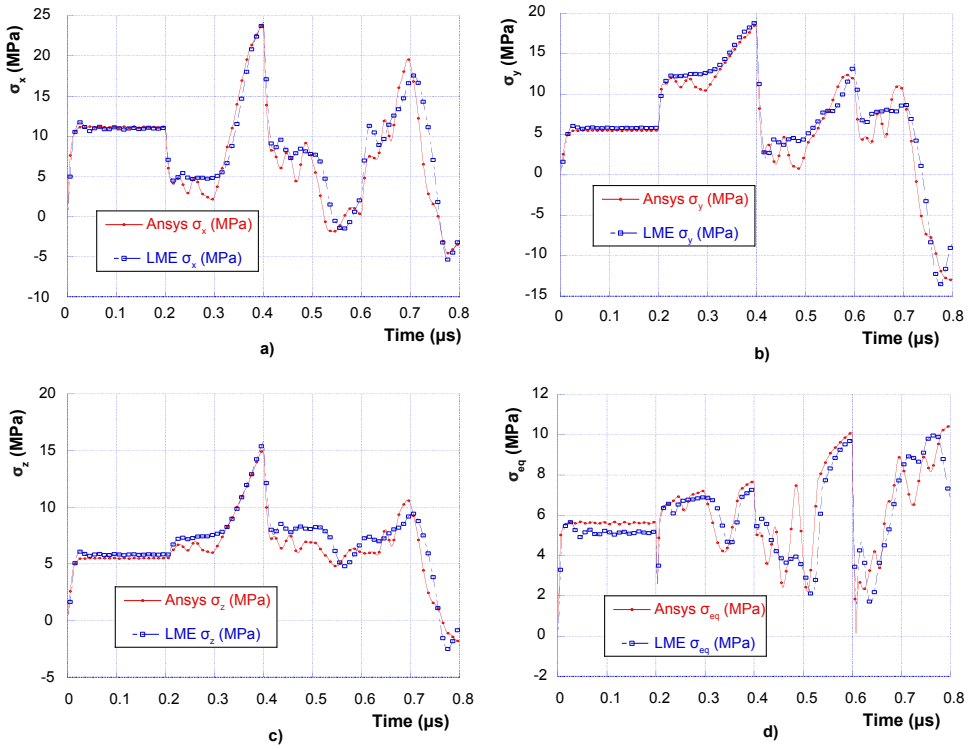

FIGURE 8 Evolution of the Cauchy stress tensor, localized at point P, along the time for both Ansys and the proposed methodology, plotting σ_x (a), σ_y (b), σ_z (c) and the von-Mises stress (d).

3.3 | Validation of the Drucker-Prager failure criterion

In the Drucker-Prager failure criterion, friction and dilatancy angles appear, which represent the main difference with respect to von-Mises. With the aim of verifying the good performance of the model, a wide range of these angles have been tested. The comparison is made with Ansys (outer cone parameters), for the results obtained under simple shear and pure shear conditions

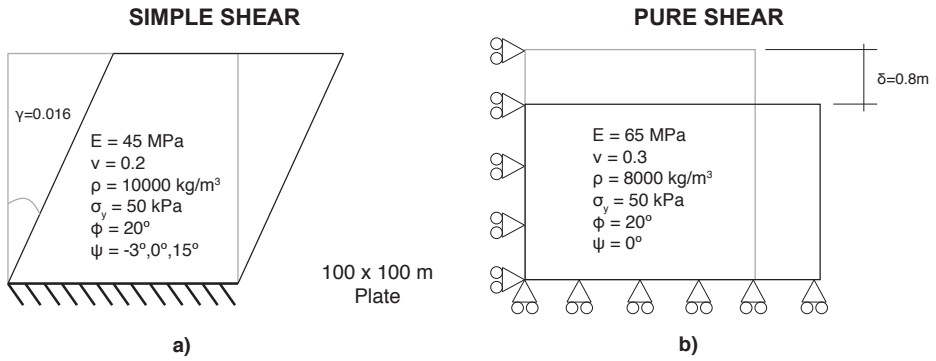

FIGURE 9 Geometry and material parameters for simple shear and pure shear problem. a) Simple shear conditions. b) Pure shear conditions.

TABLE 3 Failure stress for the Pure Shear problem

	Tension [MPa]	
	$\psi = 45$	$\psi = 0$
Hamlaoui[28]	0.0415	0.0395
LME	0.0415	0.0396
	Compression [MPa]	
	$\psi = 45$	$\psi = 0$
Hamlaoui[28]	-0.240	-0.185
LME	-0.240	0-0.165

(both compression and tension). In Fig. 9 the geometry and material parameters of both problems are presented.

Fig. 10 shows the variation of plastic and elastic strain and the stress for friction $\phi = 20°$ and three different dilatancy angles. The comparison yields similar results for 15° and 0°, but the plastic strain is different for a dilatancy of -3°. The presented results are reliable because the addition of plastic and elastic strain provides the imposed shear strain, which is not observed in Ansys results. This fact shows the robustness of the presented model even when the dilatancy angle is low or even smaller than zero, which is usually unstable as we can see in the results obtained with Ansys.

In Figs. 11 and 12 the results for pure shear conditions are shown. This model fits perfectly with the results obtained with Ansys. In this case both compression and tension have been analysed and presented in Fig. 11 . On the other hand, the behaviour using the plane strain cone is relevant because of the plane strain shallow foundations problems analysed in Section 4. In this other case, we can see the results in Fig. 12 . Hamlaoui *et al.*[28] presented the same results for a static case. The associated plasticity presents more stability than the non-associated, which is more clearly seen in compression. The comparison over time is not relevant, but the values of the failure stress, given in Tab. 3 , are important for addressing the good performance of the proposed methodology.

3.4 | Validation of the master-slave contact algorithm: the Taylor bar problem

Taylor[66] proposed the analysis of specimens deformed at very high strain rates in order to find the dynamic compressive strength of a material. These experiments involved the propagation of plastic deformation as a wave process. Fig.13 a shows a specimen deformed dynamically, such as the one produced by the impact of the cylinder against a rigid wall. A cylinder projectile of length L impacts a target at a velocity of 227 m/s. Thus, the elastic wave is faster than the plastic one and moves

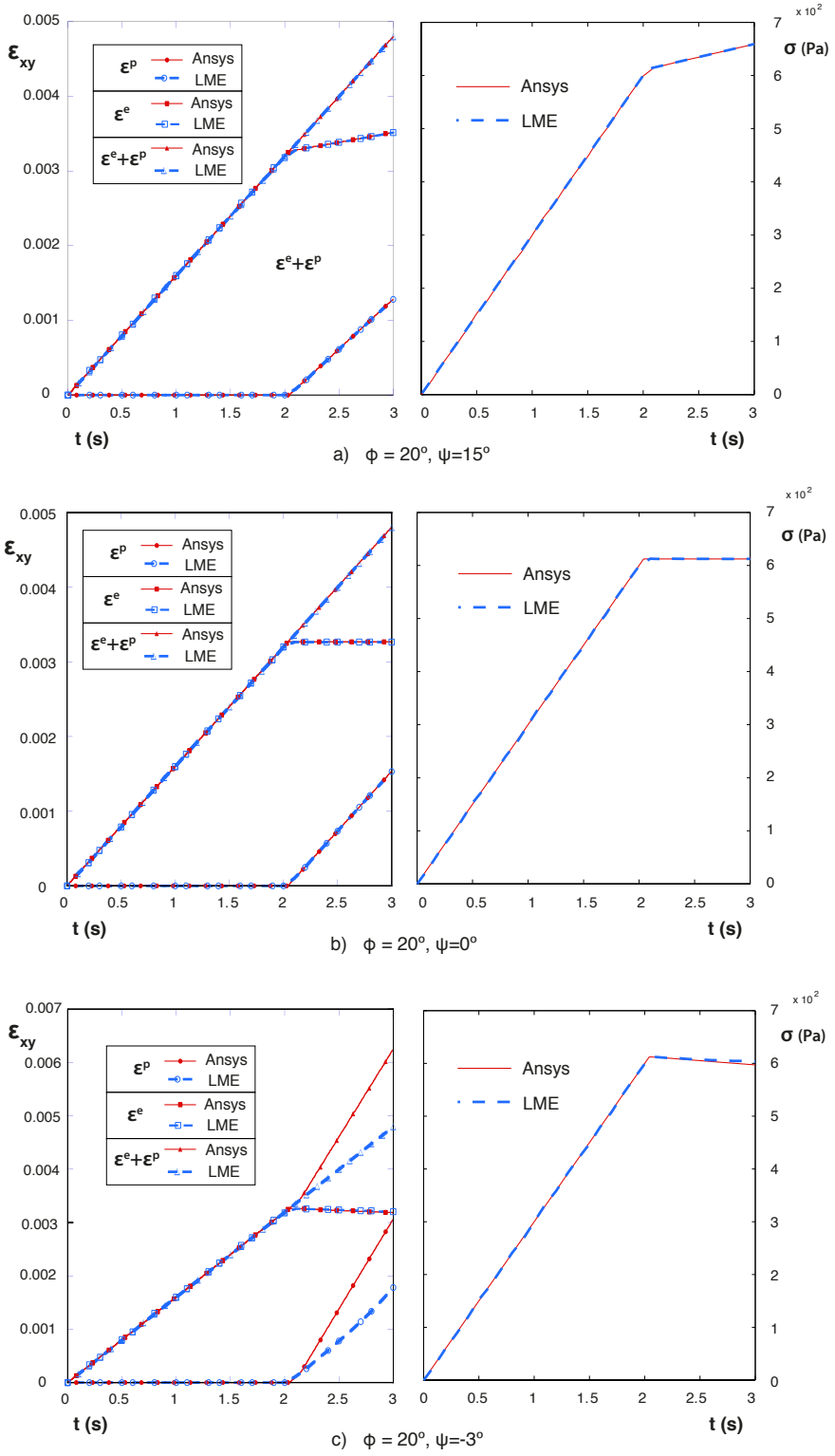

FIGURE 10 Variation of plastic and elastic strain and the stress for different friction and dilatancy angles.

at a wave speed C. This elastic compressional wave travels until it reaches the back surface of the projectile, reflects there, and then returns as a tensile wave. Finally it returns to the plastic wave, interacts with it and this triggers the end of the deformation

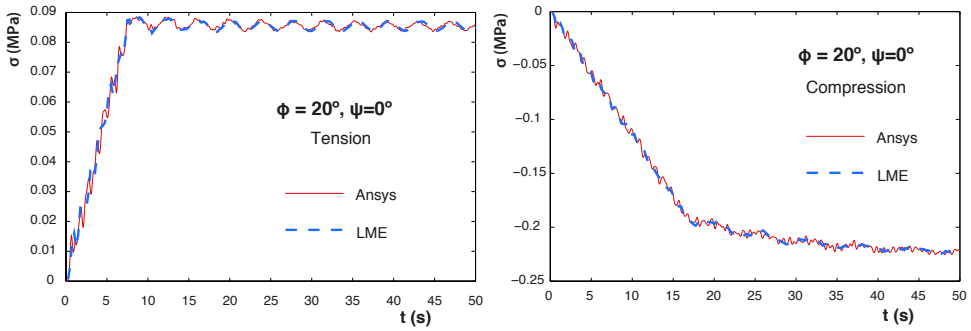

FIGURE 11 Comparison of the results of the pure shear problem with outer cone parameters between Ansys and the proposed model.

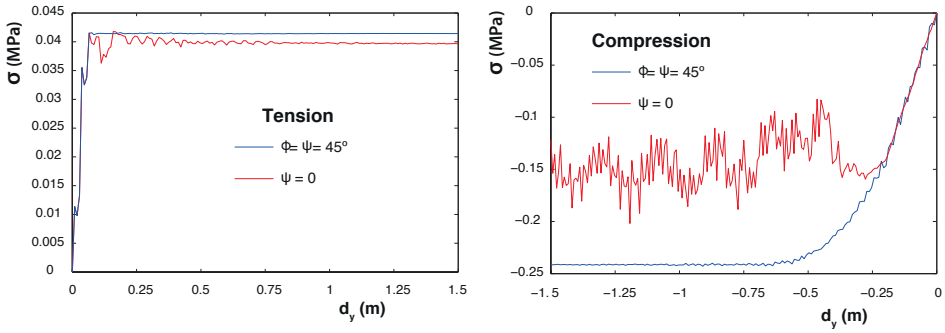

FIGURE 12 Pure shear results for the plane strain cone parameters for both compression and tension with different dilatancy angles.

process. The stress within the region sustaining plastic deformation is assumed to be constant and equal to the yield stress of the material with that strain rate. Li *et al.* in OTM[2] as well as Rodriguez *et al.* with the PFEM methodology are some examples of researches that validated their contact algorithms within this example. In Fig.13 a the material parameters used in this worked out example are provided. The geometry is axisymmetric and the simulated time is 80 μs. The final mushroom length is 6.2 mm and the evolution of the height up to 21 mm is shown in Fig.13 b, which is compared with the solution presented by Li *et al.*[2], thereby showing perfect agreement. In Fig.14 , the evolution of the equivalent plastic strain along the time is illustrated.

4 | APPLICATION TO SHALLOW FOUNDATIONS

In this Section, the methodology developed in Section 2 is applied to solve the problem of shallow foundations following the von-Mises or Drucker-Prager failure criteria.

4.1 | Strip footing loading using von-Mises failure criterion

This classic problem has been extensively used to verify the solutions provided by numerical models. The two main features to compare are the load and mechanism at failure. These results have been previously presented in the work of Blanc and Pastor[19] (among others), where the loading is applied as an incremental velocity downwards at the base of the strip footing. In

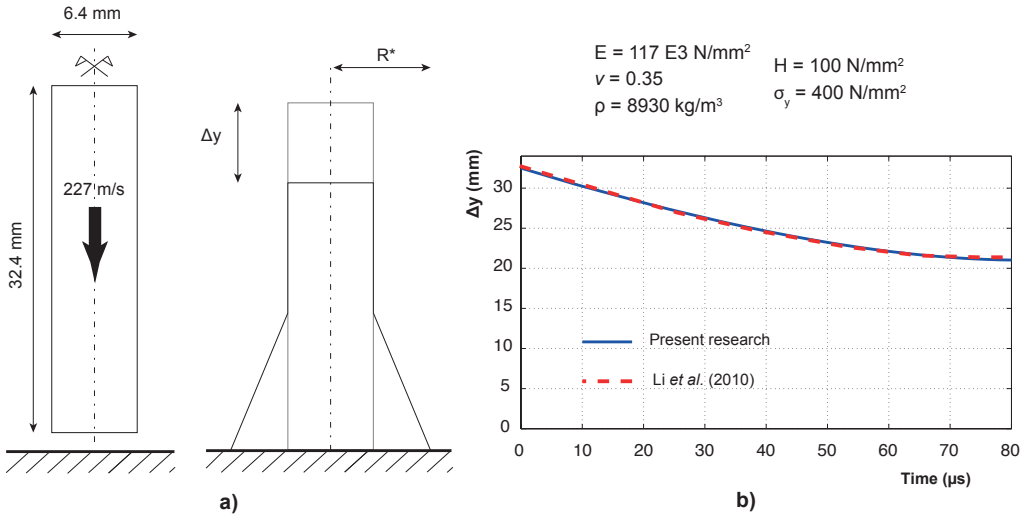

FIGURE 13 Taylor bar problem: a) geometry, material parameters and loading conditions; b) evolution of the height of the bar over time.

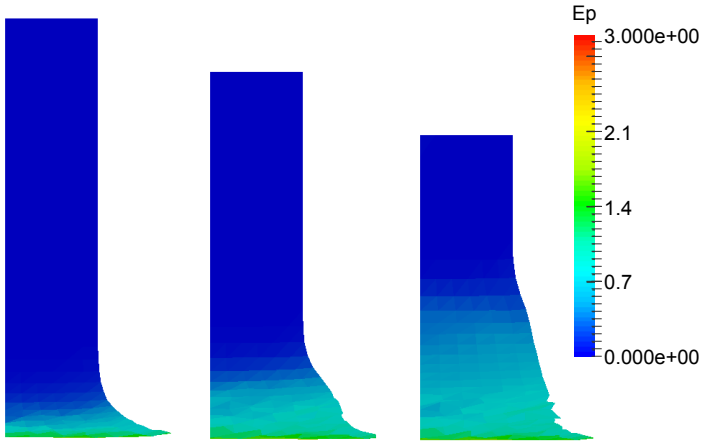

FIGURE 14 Taylor bar: equivalent plastic strain at 20, 40 and 80 μs.

the present research, the loading is applied as a negative displacement according to the following expression: $u_y = u_f \left(t/t_f\right)^2$, where $u_f = 0.04$ m. and $t_f = 4$ s. The geometry and soil parameters can be seen in Fig.15 a.

An analytical equation to obtain the load at failure is available:

$$P_{analytical} = \frac{(2+\pi)b\sigma_y}{\sqrt{3}}$$

where σ_y denotes the vertical average normal stress below the footing and b is its width. The calculation of the failure load in the computational analysis is carried out along the top material points immediately below the surface, mp, as follows:

$$P_{comp} = \sum_{i=1}^{mp} \sigma_y^i \mid x_i - x_{i-1} \mid \qquad \forall i \in \Gamma_1$$

where σ_y^i denotes the vertical stress in the material point i, and $\mid x_i - x_{i-1} \mid$ represents the length of footing corresponding to that material point, where the average vertical normal stress is assumed to be nearly σ_y^i. If no hardening or softening is assumed

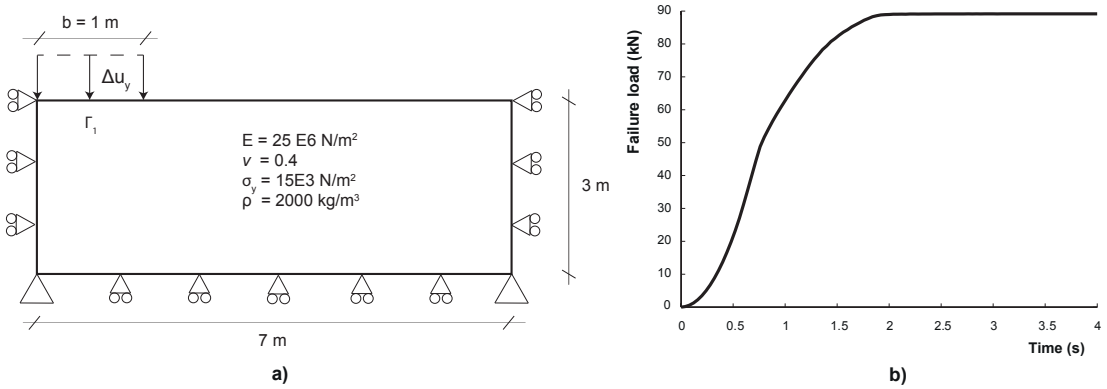

FIGURE 15 Geometry, material parameters and loading conditions of the strip footing problem.

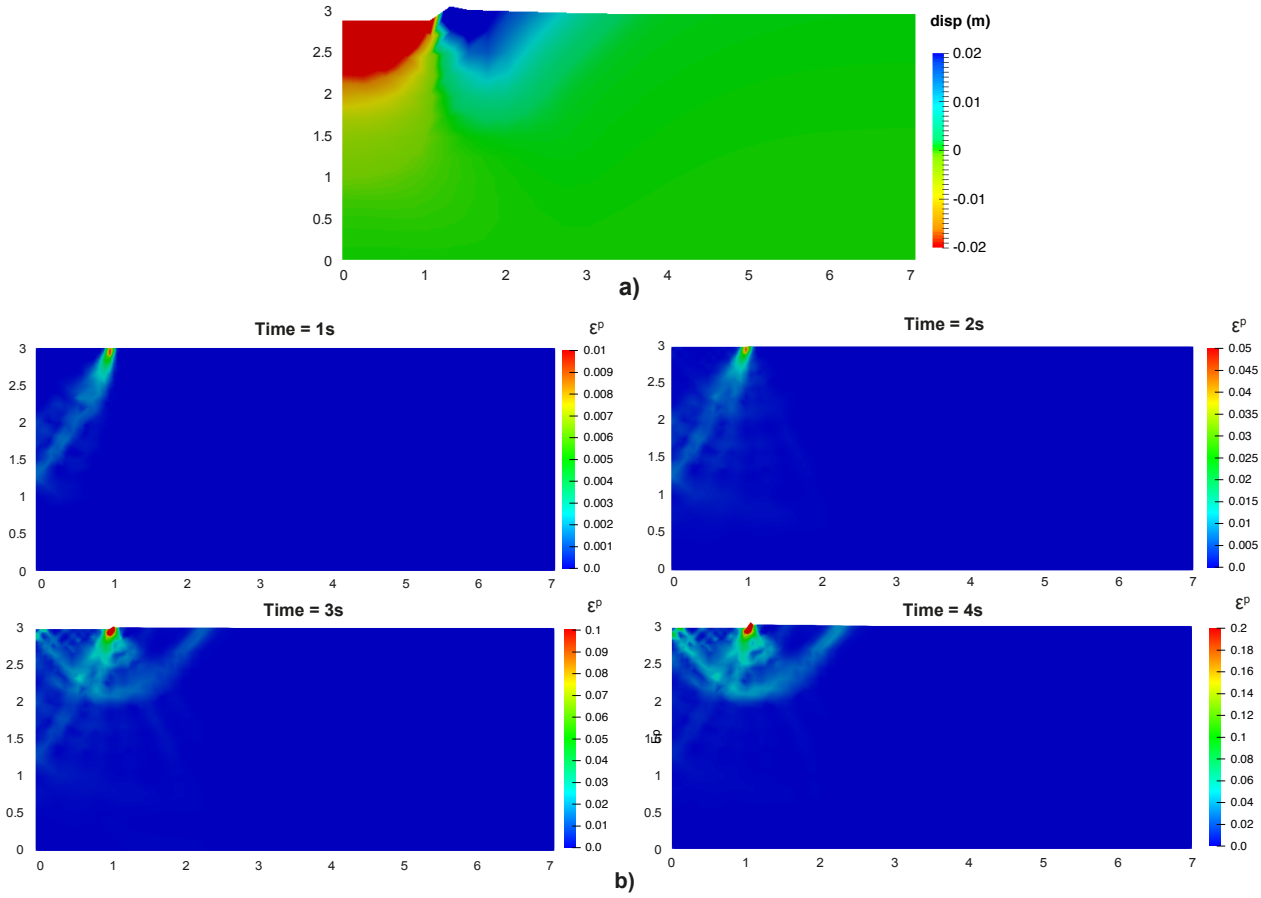

FIGURE 16 Problem of the strip footing using von-Mises law with softening. a) Deformed domain at 4 seconds; b) Equivalent plastic deformation of the strip footing failure at different simulation steps. (displacements in meters).

in the plastic model, this equation provides a very similar failure load solution in comparison with the one obtained by Blanc and Pastor[19], which is 89027 N. Compared with the analytical solution, 90650 N, our value, 89170 N, is in agreement and even closer. The progress of this calculation is depicted in Fig. 15 b. On the other hand, if we apply a softening modulus of

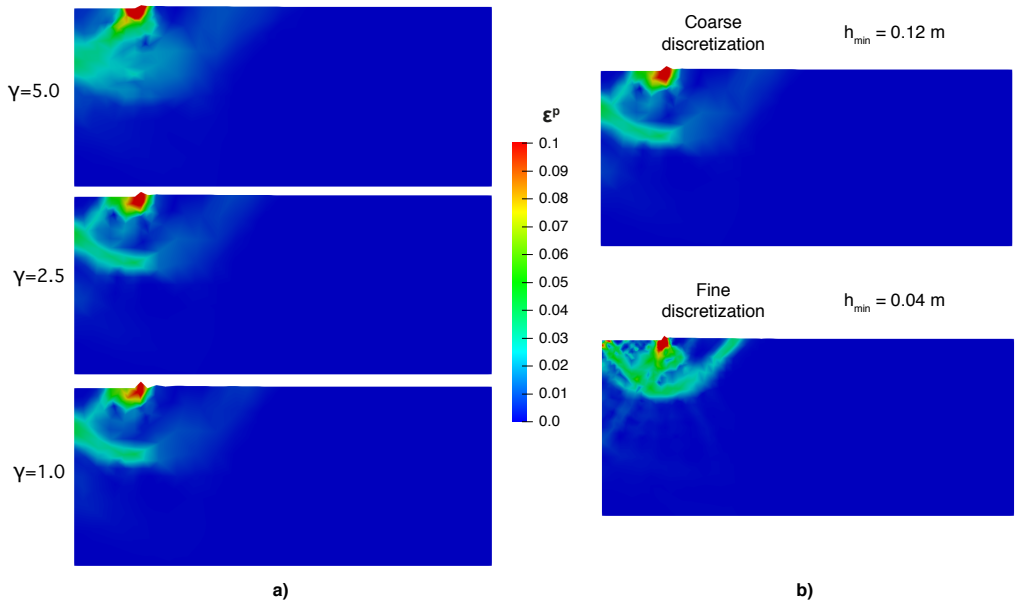

FIGURE 17 Equivalent plastic deformation of the strip footing failure using von-Mises law with softening at 4 seconds with: a) Different values of $\gamma^* = \beta h^2$ b) Two levels of discretization.

$H = -10^4$ Pa, the shear bands for the failure can be more easily formed, which is observed in Fig. 16 . This solution is obtained through a parametric analysis that is described next.

The ocurrence of the shear band is an important issue when dealing with meshfree methodologies, since these techniques employ a connectivity larger than traditional Finite Element methods. The parameter that controls the size of the neighborhood is γ^* (Eq. (6)). Arroyo and Ortiz [1] studied the influence of this parameter, concluding that the bigger is this parameter the smaller is the neighborhood. Thus, the influence of three different values of γ^* has been analyzed within the definition of the shear band with a coarse discretization. We can conclude from Fig. 17 .a that the better shape of the shear band, at least in the right part, is obtained with smaller neighborhoods, *i.e.*, with high values of γ^*.

On the other hand, in order to avoid the dependence on this parameter, the level of discretization is increased. In Fig. 17 .b it is observed that the shear band is properly captured with a finer discretization. From these results we think that there is a dependence on the discretization and the neighborhood. Thus, the refinement of the mesh during the calculation as well as the reorientation of the neighborhood in the direction of the strain seem to be good techniques to implement in order to improve the presented results in future work.

In order to verify the performance of the full model, different viscous parameters have been employed in the calculation of the failure load of the strip footing. Establishing the viscous parameter μ as 500 s, different values of the sensitivity parameter ϵ between 0.5 and 0 were tested. In Fig.18 a, the results for different values of ϵ are shown when the displacement is applied for 1 s. The larger the value of the ϵ parameter, the higher the final loading is obtained from the footing, as expected from the viscous Perzyna's model. In addition, a wide range of loading rates have been tested for ϵ equal to 0.25 (Fig.18 b) and 0.5 (Fig.18 c). It can be observed that the highest velocities lead to hardening of the material, and thus, higher failure loads.

4.2 | Drucker-Prager solution for the strip footing loading using contact algorithm

This last application involves all the features presented in this paper. The full Drucker-Prager model solution together with the contact algorithm are presented. Three different dilatancy angles are tested as well as different values of the cohesion and the friction in order to calibrate the behavior of the soil depending on its properties. The traditional way to solve this problem is the application of an imposed vertical displacement or velocity in the location of the loading. Of course, this solution makes the footing totally stiff, which permits obtaining solutions closer to the analytical one, but it is far from a real situation. In our case,

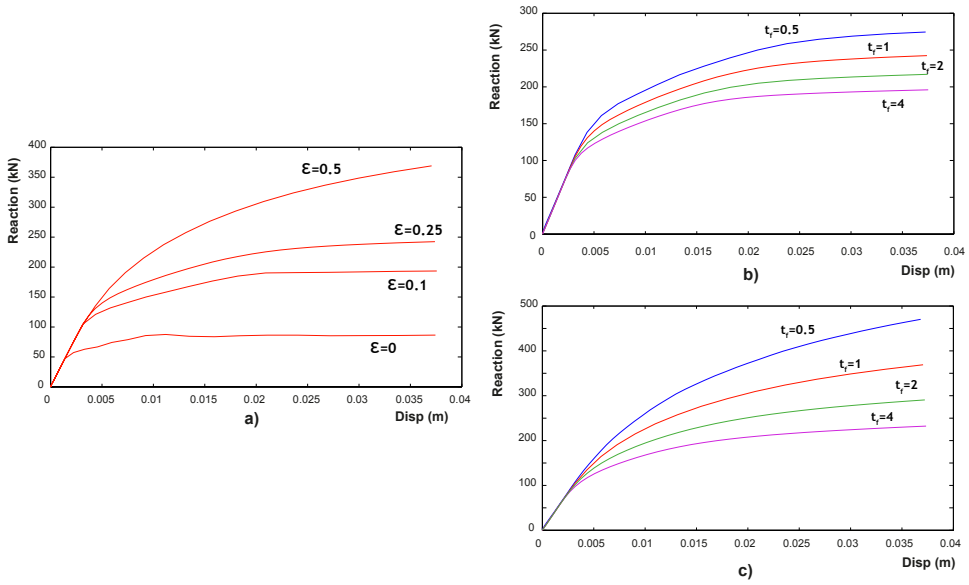

FIGURE 18 Problem of the strip footing using viscoplastic von-Mises law. a) Obtained reaction with different ϵ parameters when the displacement is imposed in 1 second; and ultimate failure load obtained for different times of displacement application with b) $\epsilon = 0.25$ and c) $\epsilon = 0.5$.

a real strip footing is modeled, on top of which the displacement is imposed. In Fig. 19 a) we can see the modeled geometry and its parameters.

The different results with variable dilatancy angle are depicted in Fig. 19 b-d. It is worth noting how the soil behaves in three different ways depending on this value. On the one hand, it can be observed how a higher dilatancy causes higher and localized heave nearby the footing, whereas when this value decreases, the effect of the loading causes smaller and more spreaded strains. Keeping dilatancy equal to 0 and varying the friction we can observe, in Fig. 19 e) that the deformation pattern does not change. However, when the cohesion is reduced, the localized heave close to the loading area tends to disappear (see Fig. 19 f)).

The reaction curve presented in Fig. 19 f) also indicates the dependency on the soil parameter. For the same cohesion and friction the reaction reaches a peak value around 160 kPa, that remains constant for dilatancy equal to zero. Nevertheless, the bigger the dilatancy the higher the reduction of the soil stiffness. And, as expected, reducing both friction and cohesion yields also the reduction of the bearing capacity, although this value remains almost constant when the dilatancy is null.

It is also worth mentioning that, in spite of the high strain level, with settlements of around 0.2 m, the solutions are very stable, demonstrating the robustness of the proposed numerical scheme for this kind of problems.

5 | CONCLUSIONS

The OTM framework, together with the Drucker-Prager criterion (following the implementation by Sanavia *et al*[30]) and the master-slave contact algorithm, is for the first time employed for geotechnical problems subjected to large deformations. Novel aspects include the F-Bar methodology to avoid locking under high compression, a remapping algorithm for the modified Nelder-Mead simplex method to ensure convergence for the calculation of the Local Max-Ent shape functions when very large deformation is involved and a master-slave contact algorithm to obtain more realistic solutions. The model has been validated against the commercial software Ansys with excellent results. The F-bar efficiency is validated through the classical Cook's membrane problem and the compression of a rectangular rubber block. The efficiency of the master-slave contact algorithm is demonstrated through the Taylor bar compression problem.

For the application to shallow foundations, the developed methodology is first compared with analytical solutions using the von-Mises yield criterion and excellent agreement has been achieved. Subsequently, the Drucker-Prager failure criterion is employed for the dynamic loading of a strip footing for three different dilatancy angles. In this case, the contact between the

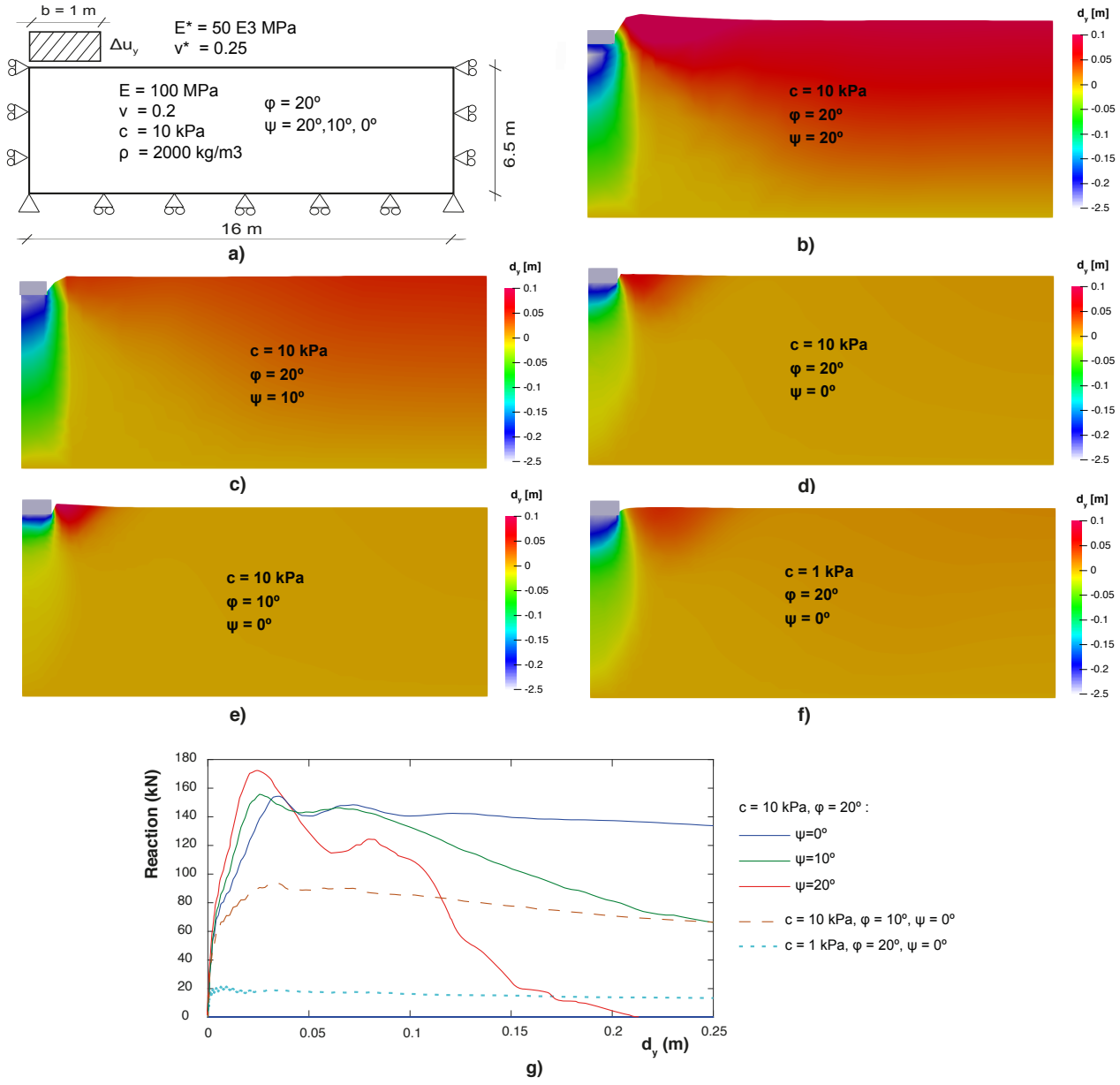

FIGURE 19 Strip footing applying the Drucker-Prager model, $\phi = 20$ degree and cohesion $c = 10kPa$. a) Geometry and properties of the material. b) Vertical displacements at failure for $\psi = 0$ degree. c) Idem for $\psi = 10$ degree. d) Idem for $\psi = 20$ degree. e) Idem for $\psi = 0$ and $\phi = 10$ degrees. f) Idem for $\psi = 0$ and $\phi = 20$ degrees and cohesion $c = 1kPa$. g) Evolution of the reaction with the vertical displacement below the footing.

footing and soil is well represented. Three very different behaviors are observed, i.e., the slope in the passive zone increases as the dilatancy angle increases.

The developed OTM meshfree methodology, validated through applications to shallow foundations, provides a generic framework for geotechnical problems in large deformation regime. Moreover, it can be further extended with the construction of non-isotropic shape functions to better capture plastic shear bands.

ACKNOWLEDGMENTS

The financial support to develop this research from the *Ministerio de Ciencia e Innovación*, under Grant Numbers, BIA2012-31678 and BIA2015-68678-C2-1-R, Spain, is greatly appreciated. The first author also acknowledges the fellowship BES2013-0639.

References

1. Arroyo M., Ortiz M. Local maximum-entropy approximation schemes: a seamless bridge between finite elements and meshfree methods. *International Journal for Numerical Methods in Engineering.* 2006; 65(13):2167–2202.
2. Li B., Habbal F., Ortiz M. Optimal transportation meshfree approximation schemes for fluid and plastic flows. *International Journal for Numerical Methods in Engineering.* 2010; 83:1541–1579.
3. Navas P. Meshfree methods applied to dynamic problems in materials in construction and soils. PhD thesis. University of Castilla-La Mancha. 2017.
4. Nelder J.A., Mead R. A simplex method for function minimization. *Computer Journal.* 1965; 7:308–313.
5. Navas P., López-Querol S., Yu R.C., Li B. B-bar based algorithm applied to meshfree numerical schemes to solve unconfined seepage problems through porous media. *International Journal for Numerical and Analytical Methods in Geomechanics.* 2016; 40:962–984.
6. Navas P., Yu R.C., López-Querol S., Li B. Dynamic consolidation problems in saturated soils solved through u-w formulation in a LME meshfree framework. *Computers and Geotechnics.* 2016; 79:55–72.
7. Camacho G.T., Ortiz M. Adaptive Lagrangian modelling of ballistic penetration of metallic targets. *Computers methods in applied mechanics and engineering.* 1997; 142:269–301.
8. Prandtl L. Über die Härte plastischer Körper. Nachrichten von der Gesellschaft der Wissenschaften zu Göttingen. *Mathematisch-Physikalische Klasse.* 1920; 74–85.
9. Prandtl L. Zum Erddruckproblem. In C. B. Biezeno & J. M. Burgers (Eds.). *Proceedings of 1st International Congress for applied mechanics.* 1924; 295–311.
10. Griffiths D.V. Computation of bearing capacity factors using finite elements. *Géotechnique.* 1982; 32:195–202.
11. Borst R., Vermeer P.A. Possibilities and limitations of finite elements for limit analysis. *Géotechnique.* 1984; 34:199–210.
12. Drescher A., Detournay E. Limit load in translational mechanisms for associative and non-associative materials. *Géotechnique.* 1993; 43:443–456.
13. Manoharan N., Dasgupta S.P. Bearing capacity of surface footings by finite elements. *Computers and structures.* 1995; 54:563–568.
14. Frydman S., Burd H.J. Numerical studies of bearing capacity factor Nc.. *Journal of Geotechnical and Geoenvironmental Engineering ASCE.* 1997; 123:20–29.
15. Yin J., Wang Y., Selvadurai A. Influence of non-associative on the bearing capacity of a strip footing. *Journal of Geotechnical and Geoenvironmental Engineering ASCE.* 2001; 127:958–989.
16. Erickson H.L., Drescher A. Bearing capacity of circular footings. *Journal of Geotechnical and Geoenvironmental Engineering ASCE.* 2002; 128:38–43.
17. Monforte L., Arroyo M., Carbonell J.M., Gens A. Numerical simulation of undrained insertion problems in geotechnical engineering with the particle finite element method (PFEM). *Computers and Geotechnics.* 2017; 82:144–156.

18. Solowski W.T., Sloan S.W. Evaluation of material point method for use in geotechnics. *International Journal for Numerical and Analytical Methods in Geomechanics.* 2015; 39(7):685–701.

19. Blanc T., Pastor M. A stablized Runge-Kutta, Taylor smoothed particle hydrodynamics algorithm for large deformation problems in dynamics. *International Journal for Numerical Methods in Engineering.* 2012; 91:1427–1458.

20. Cundall P.A., Strack O.D.L. A discrete numerical model for granular assemblies. *Geotechnique.* 1979; 1:47–65.

21. Arroyo M., Butlanska J., Gens A., Calvetti F., Jamiolkowski M. Cone penetration tests in a virtual calibration chamber. *Geotechnique.* 2011; 6:525–531.

22. Loukidis D., Salgado R. Bearing capacity of strip and circular footings in sand using finite elements. *Computers and Geotechnics.* 2009; 36:871–879.

23. Berga A., Saxcé G. Elastoplastic finite element analysis of soil problems with implicit standard material constitutive laws. *Revue Européenne des Eléments finis.* 1994; 3:411–456.

24. Hjiaj M., Fortin J., Saxcé G.. A Complete stress update algorithm for the non-associated Drucker–Prager model including treatment of the apex. *International Journal of Engineering Science.* 2003; 41:1109–1143.

25. Hjiaj M., Lyamin A. V., Sloan S. W.. Numerical limit analysis solutions for the bearing capacity factor Ny. *International Journal of Solids and Structures.* 2005; 42:1681–1704.

26. Berga A. Mathematical and numerical modeling of the non-associated plasticity of soils–Part 1: The boundary value problem. *International Journal of Non-Linear Mechanics.* 2012; 47:26–35.

27. Berga A. Mathematical and numerical modeling of the non-associated plasticity of soils–Part 2: Finite element analysis. *International Journal of Non-Linear Mechanics.* 2012; 47:36–45.

28. Hamlaoui M., Oueslati A., B. Lamri, Saxcé G. Finite element analysis of the plastic limit load and the collapse mechanism of strip foundations with non-associated Drucker-Prager model. *European Journal of Environmental and Civil Engineering.* 2015; 19(10):1179–1201.

29. Sanavia L., Schrefler B.A., Steinmann P. A formulation for an unsaturated porous medium undergoing large inelastic strains. *Computational Mechanics.* 2002; 28:137–151.

30. Sanavia L., Pesavento F., Schrefler B.A. Finite element analysis of non-isothermal multiphase geomaterials with application to strain localization simulation. *Computational Mechanics.* 2006; 37(4):331–348.

31. Lazari M., Sanavia L., Schrefler B.A. Local and non-local elasto-viscoplasticity in strain localization analysis of multiphase geomaterials. *international Journal for Numerical and Analytical methods in Geomechanics.* 2015; 39:1570–1592.

32. Cuitiño A., Ortiz M. A material-independent method for extending stress update algotithms from small-strain plasticity to finite plasticity with multiplicative kinematics. *Engineering computations.* 1992; 9:437–451.

33. Gingold R.A., Monaghan J.J. Smoothed particle hydrodynamics - Theory and application to non-spherical stars. *Monthly Notices of the Royal Astronomical Society.* 1977; 181:375-389.

34. Blanc T., Pastor M. A stablized Smoothed Particle Hydrodynamics, Taylor-Galerkin algorithm for soil dynamics problems. *International Journal for Numerical and Analytical Methods in Geomechanics.* 2013; 37:1–30.

35. Fan H., Bergel G.L., Li S. A hybrid peridynamics-SPH simulation of soil fragmentation by blast loads of buried explosive. *International Journal of Impact Engineering*, 2016; 87:14–27.

36. Bui H.H., Fukagawa R. An improved SPH method for saturated soils and its application to investigate the mechanisms of embankment failure: Case of hydrostatic pore-water pressure. *International Journal for Numerical and Analytical Methods in Geomechanics.*, 2013; 37:31–50.

37. Sulsky D., Chen Z., Schreyer H.L. A particle method for history-dependent materials. *Computer Methods in Applied Mechanics and Engineering.* 1994; 118:179–196.

38. Bandara S., Soga K. Coupling of soil deformation and pore fluid flow using material point method. *Computers and Geotechnics.* 2015; 63:199–214.

39. Alonso E.E., Zabala F. Progressive failure of Aznalcóllar dam using the material point method. *Géotechnique* 2011; 61(9):795–808.

40. Ceccato F., Beuth L., Vermeer P.A., Simonini P. Two-phase Material Point Method applied to the study of cone penetration. *Computers and Geotechnics* 2016; 80:440–452

41. Hu Y., Randolph M.F. H-adaptive FE analysis of elasto-plastic non-homogeneous soil with large deformation. *Computers and Geotechnics* 1998; 23(1):61–83.

42. Lu Q., Randolph M.F., Hu Y., Bugarski I.C. A numerical study of cone penetration in clay. *Geéotechnique* 2004; 54(4):257–67.

43. Zhou H., Randolph M.F.. Numerical investigation into cycling of full-flow penetrometers in soft clay. *Geéotechnique* 2009; 59(10):801–12.

44. Nazem M., Sheng D., Carter J.P. Stress integration and mesh refinement for large deformation in geomechanics. *International Journal for Numerical Methods in Engineering* 2006; 65(7):1002–27.

45. Nazem M., Carter J.P., Airey D.W., Chow S.H. Dynamic analysis of a smooth penetrometer free-falling into uniform clay. *Geéotechnique* 2012; 62 (10):893–905.

46. Walker J., Yu H.S. Adaptive finite element analysis of cone penetration in clay. *Acta Geotechnica* 2006; 1(1):43âĂŞ57.

47. Wang D., Bienen B., Nazem M., Tian Y., Zheng J., Pucker T., *et al.* Large deformation finite element analyses in geotechnical engineering. *Computers and Geotechnics* 2015; 65:104–14.

48. Monforte L, Carbonell J. M., Arroyo M., Gens A.. Performance of mixed formulations for the particle finite element method in soil mechanics problems. *Computational Particle Mechanics.* 2017; 4(3):269–284.

49. Ortiz A., Puso M.A., Sukumar N. Construction of Polygonal Interpolants: A Maximum Entropy Approach. *International Journal for Numerical Methods in Engineering.* 2004; 61(12):2159–2181.

50. Wiˆkezckowski Z. The material point method in large strain engineering problems. *Computational Methods Applied Mechanics and Engineering.* 2004; 193:4417–4438.

51. Bonet J., Wood R.D. *Nonlinear continuum mechanics for finite element analysis*. Cambridge University Press,The Pitt Building, Trumpington Street, Cambridge, UK; 1997.

52. Souza Neto E.A., Perić D., Owen D.R.J. *Computational methods for plasticity*. John Wiley & Sons Ltd., The Atrium, Southern Gate, Chichester, UK; 2008.

53. Taylor L., Flanagan D. PRONTO 2D: A two-dimensional transient solid dynamics program. *Sandia National Laboratories.* 1987; SAND86-0594.

54. De Souza Neto E.A., Pires F.M., Owen D.R.J. F-bar-based linear triangles and tetrahedra for finite strain analysis of nearly incompressible solids. Part I: formulation and benchmarking. *International Journal for Numerical Methods in Engineering.* 2005; 62:353-383.

55. Elguedj T., Bazilevs Y., Calo V. M., Hughes T.J.R. $\overline{B}$ and $\overline{F}$ projection methods for nearly incompressible linear and non-linear elasticity and plasticity using higher-order NURBS elements. *Computer Methods in Applied Mechanics and Engineering*. 2008; 197(33-40):2732-2762.

56. Martínez M.A. Métodos de búsqueda directa para optimizacioón sin derivadas. PhD thesis. Universidad Nacional de Córdoba. 2014.

57. De Souza Neto E.A., Perić D., Dutko M., Owen D.R.J. Design of simple low order finite elements for large strain analysis of nearly incompressible solids. *International Journal of Solids and Structures.* 1996; 33:3277-3296.

58. Simo J.C., Taylor R.L., Pister K.S. Variational and projection methods for the volume constraint in finite deformation elasto-plasticity. *Computer Methods in Applied Mechanics and Engineering.* 1985; 51:177-208.

59. Simo J.C., Taylor R.L. Quasi-incompressible finite elasticity in principal stretches. Continuum basis and numerical algorithm. *Computer Methods in Applied Mechanics and Engineering.* 1991; 85:273-310.

60. ANSYS. *Structural analysis guide – ANSYS user manual – release 12.0.* Canonsburg, Pensilvania, USA: Ansys, Inc.; 2009.

61. Simo J.C., Rifai M.S. A class of mixed assumed strain methods and the method of incompatible modes. *International Journal for Numerical Methods in Engineering.* 1990; 29:1595-1638.

62. Kasper E.P., Taylor R.L. A mixed-enhanced strain method: Part I: Geometrically linear problems. *Computers and Structures.* 2000; 75(3):237-250.

63. Hauret P., Kuhl E., Ortiz M. Diamond elements: A finite element/discrete-mechanics approximation scheme with guaranteed optimal convergence in incompressible elasticity. *International Journal for Numerical Methods in Engineering.* 2007; 73:253-294.

64. Artioli E., Castellazzi G., Krysl P. Assumed strain nodally integrated hexahedral finite element formulations for elastoplastic applications. *International Journal for Numerical Methods in Engineering.* 2014; 99(11):844-866.

65. De Souza Neto E.A., Pires F.M., Owen D.R.J. Enhanced lower-order element formulations for large strains. *In Computational Plasticity: Fundamentals and Applications, Proceedings of the Fourth International Conference held in Barcelona, Owen DRJ, Oñate E, Hinton E (eds). 3rd–6th April 1995.*1995; 293-320.

66. Taylor G. The use of flat-ended projectiles for determining dynamic yield stress. I. theoretical considerations. *Proceedings of the Royal Society of Mathematical, Physical and Engineering Science.* 1948; 194:289–299.

67. Rodriguez J. M., Carbonell J. M., Cante J. C., Oliver J. The particle finite element method (PFEM) in thermo-mechanical problems. *International Journal for Numerical Methods in Engineering.* 2016; 107(9):733–785.

68. López-Querol S., Blazquez R. Liquefaction and cyclic mobility model in saturated granular media. *International Journal for Numerical and Analytical Methods in Geomechanics.* 2006; 30:413–439.

How to cite this article: P. Navas, S. López-Querol, R.C. Yu, and M. Pastor (2017), Geotechnical Optimal Transportation Meshfree: application to large deformation analysis of shallow foundations, *Int J Numer Methods Eng*, *2017;00:1–6*.

Algorithm 1 Modified Nelder-Mead

Input: *dim+1* vertexes: $v_1,\ v_2,\ \dots,\ v_{dim},\ v_{dim+1}$ and the values of the objective function f in these points $f(v_1) \leq f(v_2) \leq \dots \leq f(v_{dim}) \leq f(v_{dim+1})$
Ouput: $v_i^{k+1} \mid f(v_1^{k+1}) - f(v_{\dim+1}^{k+1})$<tolerance

While: $f(v_1^{k+1}) - f(v_{\dim+1}^{k+1})$>tolerance

1. **Order:** Vertexes are ordered according to the value of the objective value.

$$v_1,\ v_2,\ \dots,\ v_{dim},\ v_{dim+1}$$

So that, $f(v_1) \leq f(v_2) \leq \dots \leq f(v_{dim}) \leq f(v_{dim+1})$

2. **Spin:** (innovation respect past methodologies)

While: $von < \tau$

- Turn the vertexes: Fig.1 .B. where $\Delta d = diam(S)/10$.
- Calculate normalized volumes *von* (Eq.7) of different proposed new simplexes.
- Choose the smallest *von*

3.**Reflection:**

Gravity center: $\overline{v} = \frac{1}{\dim} \sum_{i=1}^{\dim} v_i$

Reflected point: $v_r = \overline{v} + \rho(\overline{v} - v_{\dim+1})$

Evaluation:

- If $f(v_r) < f(x_1)$: Go to 4.
- If $f(v_r) > f(x_1)$ but $f(v_r) < f(x_{dim})$: Go to 1.
- If $f(v_r) > f(x_{dim})$: Go to 5.

4. **Expansion**

Expended point: $v_e = \overline{v} + \chi(v_r - \overline{v})$

If $f(v_e) < f(v_r)$ $v_r = v_e$

else, discard v_e and take v_r

5. **Contraction**: two possibilities

If $f(v_r) < f(v_{\dim+1})$ External contraction: $v_c = \overline{v} + \gamma(v_r - \overline{v})$

If $f(v_c) < f(v_r)$ go to 1.

else, go to 6.

else, if $f(v_r) > f(v_{\dim+1})$ Internal contraction: $v_c = \overline{v} - \gamma(\overline{v} - v_{\dim+1})$

$f(v_c) < f(v_{\dim+1})$ go to 1.

else, go to 6.

6. **Shrinkage** and go to 1:

$$v_i^{k+1} = v_1^k + \sigma(v_i^k - v_1^k) \qquad i = 2, \dots, \dim+1$$

Algorithm 2 Explicit scheme: Newmark central difference

1. Explicit Newmark Predictor ($\gamma = 0.5$)

$$\begin{aligned} \boldsymbol{u}_{k+1} &= \boldsymbol{u}_k + \Delta t \boldsymbol{v}_k + \frac{1}{2}\Delta t^2 \boldsymbol{a}_k = \boldsymbol{u}_k + \Delta \boldsymbol{u}_{k+1} \\ \boldsymbol{v}_{k+1} &= \boldsymbol{v}_k + (1-\gamma)\Delta t \, \boldsymbol{a}_k \\ \boldsymbol{x}_{k+1} &= \boldsymbol{x}_k + \Delta \boldsymbol{u}_{k+1} \end{aligned}$$

2. Material points position update

$$\boldsymbol{x}^p_{k+1} = \boldsymbol{x}^p_k + \sum_{a=1}^{n} \Delta \boldsymbol{u}^a_{k+1} N^a(\boldsymbol{x}^p_k)$$

3. Deformation gradient calculation

$$\begin{aligned} \Delta \mathbf{F}^p_{k+1} &= I + \sum_{a=1}^{n} \Delta \boldsymbol{u}^a_{k+1} \nabla N^a(\boldsymbol{x}^p_k) \\ \mathbf{F}_{k+1} &= \Delta \mathbf{F}_{k+1} \mathbf{F}_k \end{aligned}$$

4. F-Bar calculation

$$\overline{\mathbf{F}} = \left(\frac{\overline{J}_e}{J} \right)^{1/3} \mathbf{F}$$

5. Stretches λ_i calculation: Eigenvalues of $\mathbf{C} = \mathbf{F}^T \mathbf{F}$

6. Remapping loop

- **6.1** If $\Delta \lambda_i > tolerance$ for $i = 1, 2, 3$
  - **6.1.1** Update neighborhood and parameter $\beta^p_{k+1} < \beta^p_k$ (See Eq.1 and 2)
  - **6.1.2** Recompute $N^a(\boldsymbol{x}^p_{k+1})$ and $\nabla N^a(\boldsymbol{x}^p_{k+1})$
  - **6.1.3** Go to **2.**
- **6.2** Recompute $N^a(\boldsymbol{x}^p_{k+1})$ and $\nabla N^a(\boldsymbol{x}^p_{k+1})$

7. Update density and recompute lumped mass

$$\rho_{k+1} = \frac{M}{V_{k+1}}$$

8. Visco-plastic algorithm: Algorithm 3, Visco-plastic Drucker-Prager model

9. Solver

$$\boldsymbol{a}_{k+1} = \mathbf{M}^{-1}(\boldsymbol{f}^{ext} - \boldsymbol{f}^{int})$$

10. Explicit Newmark Corrector

$$\boldsymbol{v}_{k+1} = \boldsymbol{v}_{k+1} + \gamma \Delta t \, \boldsymbol{a}_{k+1}$$

Algorithm 3 Visco-Plastic Drucker-Prager model

1. Calculation of the small strain tensor[32]

$$\mathbf{C}^{e\,trial}_{k+1} = (\mathbf{F}^{p}_{k})^{-T}\mathbf{C}_{k+1}(\mathbf{F}^{p}_{k})^{-1}$$

$$\boldsymbol{\varepsilon}^{e\,trial}_{k+1} = \frac{1}{2}\log \mathbf{C}^{e\,trial}_{k+1}$$

2. Elastic Predictor: volumetric and deviatoric stress measurements

$$\text{Volumetric: } p^{trial}_{k+1} = K\left(\varepsilon^{e}_{vol}\right)^{trial}_{k+1}$$
$$\text{Deviatoric: } \mathbf{s}^{trial}_{k+1} = 2G\left(\boldsymbol{\varepsilon}^{e}_{dev}\right)^{trial}_{k+1}$$

$$\text{being: } \boldsymbol{\sigma}^{trial}_{k+1} = J^{-1}\mathbf{F}_{k+1}\mathbf{S}^{trial}_{k+1}\mathbf{F}^{T}_{k+1}$$

3. Yield condition: Starting from incremental plastic strain equal to zero. $\Delta\gamma = 0$
If $\Phi = 3\alpha_{_F} p^{trial}_{k+1} + \|\mathbf{s}^{trial}_{k+1}\| - \beta c_k \geq 0$ Plastic region:

- **3.1.** Hardening modulus: $H = \frac{\partial c}{\partial \overline{\varepsilon}^{p}} = \frac{c_0}{n\varepsilon_0}\left(1 + \frac{\overline{\varepsilon}^{p}_{k}}{\varepsilon_0}\right)^{\left(\frac{1}{n}-1\right)}$
- **3.2.** Calculation of the limit between classic or apex algorithm: $p_{lim} = \frac{3\alpha_{_Q}K}{2G}\|\mathbf{s}^{trial}_{k+1}\| + \frac{\beta}{3\alpha_{_F}}\left(\frac{\|\mathbf{s}^{trial}_{k+1}\|}{2G}H\sqrt{1+3\alpha^{2}_{_Q}} + c_k\right)$

  If $p^{trial}_{k+1} \leq p_{lim}$ classical plastic iterator:
  - **3.2.a.1** Derivative of the yield surface:

$$d = \frac{\partial \Phi}{\partial \Delta\gamma} = -9K\alpha_{_F}\alpha_{_Q} - 2G - H\beta\sqrt{3\alpha^{2}_{_Q}+1}\left[1 + \left(\frac{\mu\Delta\gamma}{\Delta t}\right)^{\epsilon}\right] - \frac{\epsilon c_{k+1}}{\Delta\gamma}\left(\frac{\mu\Delta\gamma}{\Delta t}\right)^{\epsilon}$$

  - **3.2.a.2** Increment of plastic strain: $\Delta\gamma = \Delta\gamma - \frac{\Phi}{d}$
  - **3.2.a.3** Equivalent plastic strain: $\overline{\varepsilon}^{p}_{k+1} = \overline{\varepsilon}^{p}_{k} + \Delta\gamma\sqrt{3\alpha^{2}_{_Q}+1}$
  - **3.2.a.4** Hardening law: $c_{k+1} = c_0\left(1 + \frac{\overline{\varepsilon}^{p}_{k+1}}{\varepsilon_0}\right)^{\frac{1}{n}};\ H = \frac{\partial c}{\partial \overline{\varepsilon}^{p}} = \frac{c_0}{n\varepsilon_0}\left(1 + \frac{\overline{\varepsilon}^{p}_{k+1}}{\varepsilon_0}\right)^{\left(\frac{1}{n}-1\right)}$
  - **3.2.a.6** Yield function: $\Phi = \|\mathbf{s}^{trial}_{k+1}\| - 2G\Delta\gamma + 3\alpha_{_F}[p^{trial}_{k+1} - 3K\alpha_{_Q}\Delta\gamma] - \beta c_{k+1}\left[1 + \left(\frac{\mu\Delta\gamma}{\Delta t}\right)^{\epsilon}\right]$
  - **3.2.a.7** If $\Phi < tolerance$ go to **3.2.a.8**, else go to **3.2.a.1**
  - **3.2.a.8** Update

$$\Delta\boldsymbol{\varepsilon}^{p}_{k+1} = \alpha_{_Q}\Delta\gamma\mathbf{I} + \frac{\Delta\gamma}{\|\mathbf{s}^{trial}_{k+1}\|}\mathbf{s}^{trial}_{k+1}$$

$$\sigma_{k+1} = \left(p^{trial}_{k+1} - 3K\alpha_{_Q}\Delta\gamma\right)\mathbf{I} + \left(1 - \frac{2G\Delta\gamma}{\|\mathbf{s}^{trial}_{k+1}\|}\right)\mathbf{s}^{trial}_{k+1}$$

  else: apex plastic iterator: $\Delta\gamma_1 = \frac{\|\mathbf{s}^{trial}_{k+1}\|}{2G};\ \Delta\gamma_2 = 0$
  - **3.2.b.1** Derivative of the yield surface:

$$d = \frac{\partial \Phi}{\partial \Delta\gamma_2} = 3\alpha_{_Q}K + \frac{3H\beta\alpha^{2}_{_Q}\left(\Delta\gamma_1 + \Delta\gamma_2\right)}{3\alpha_{_F}\sqrt{\Delta\gamma^{2}_{1} + 3\alpha^{2}_{_Q}(\Delta\gamma_1 + \Delta\gamma_2)^{2}}}$$

  - **3.2.b.2** Increment of plastic strain, $\Delta\gamma_2 = \Delta\gamma_2 - \frac{\Phi}{d}$
  - **3.2.b.3** Yield function: $\Phi = \frac{\beta}{3\alpha_{_F}}\left[c_k + H\sqrt{\Delta\gamma^{2}_{1} + 3\alpha^{2}_{_Q}(\Delta\gamma_1 + \Delta\gamma_2)^{2}}\right] - p^{trial}_{k+1} + 3K\alpha_{_Q}\left(\Delta\gamma_1 + \Delta\gamma_2\right)$
  - If $\Phi < tolerance$

$$\overline{\varepsilon}^{p}_{k+1} = \overline{\varepsilon}^{p}_{k} + \sqrt{\Delta\gamma^{2}_{1} + 3\alpha^{2}_{_Q}\left(\Delta\gamma_1 + \Delta\gamma_2\right)^{2}}$$

$$\Delta\boldsymbol{\varepsilon}^{p}_{k+1} = \alpha_{_Q}\left(\Delta\gamma_1 + \Delta\gamma_2\right)\mathbf{I} + \frac{\Delta\gamma_1}{\|\mathbf{s}^{trial}_{k+1}\|}\mathbf{s}^{trial}_{k+1}$$

$$\sigma_{k+1} = \left(p^{trial}_{k+1} - 3K\alpha_{_Q}\Delta\gamma\right)\mathbf{I}$$

    else: go to **3.2.b.1**

4. Update plastic deformation gradient

$$\Delta \mathbf{F}^p_{k+1} = \exp(\Delta \boldsymbol{\epsilon}^p_{k+1})$$
$$\mathbf{F}^p_{k+1} = \Delta \mathbf{F}^p_{k+1} \mathbf{F}^p_k$$

5. Compute internal forces

$$f^{int} = \sum^{p} \int_{\Omega} \boldsymbol{\sigma}^p_{k+1} \nabla N dV$$